Nano Energy 71 (2020) 104592

Contents lists available at ScienceDirect

Nano Energy

journal homepage: http://www.elsevier.com/locate/nanoen

Full paper

Template-guided synthesis of Co nanoparticles embedded in hollow nitrogen doped carbon tubes as a highly efficient catalyst for rechargeable Zn-air batteries

Qingyan Zhou [a], Zhen Zhang [b], Jiajun Cai [a], Bing Liu [a], Yunlong Zhang [a], Xiaofei Gong [a], Xulei Sui [a], Aiping Yu [b], Lei Zhao [a,b,**], Zhenbo Wang [a,***], Zhongwei Chen [b,*]

[a] MIIT Key Laboratory of Critical Materials Technology for New Energy Conversion and Storage, School of Chemistry and Chemical Engineering, State Key Lab of Urban Water Resource and Environment, Harbin Institute of Technology, Harbin, 150001, China
[b] Department of Chemical Engineering, Waterloo Institute for Nanotechnology, Waterloo Institute for Sustainable Energy, University of Waterloo, Waterloo, Ontario, N2L 3G1, Canada

ARTICLE INFO

Keywords:
Polypyrrole
Metal-organic frameworks
Hollow nanotubes
1D hierarchical structure
Zn-air batteries

ABSTRACT

Rational design and construction of highly efficient and durable non-noble-metal bifunctional catalysts for oxygen reduction reaction (ORR) and oxygen evolution reaction (OER) is crucial to promote the widespread implementation of rechargeable Zn-air batteries. Herein, a bifunctional catalyst comprising Co nanoparticles uniformly embedded in hollow nitrogen doped carbon tubes (Co@hNCTs) is fabricated by a facile tube-directed templating strategy. In this strategy, surfactant-treated polypyrrole (PPy) nanotubes serve as the structure-guiding templates for efficient capture of Co^{2+}, realizing the in-situ growth of zeolitic imidazolate frameworks-67 (ZIF-67) nanocrystals on PPy nanotubes. Sodium laurylsulfonate acts as anionic surfactant to endow PPy nanotubes with functional electronegative surface and strong anchoring effect toward ZIF-67, playing the pivotal role in binding of ZIF-67 nanocrystals with PPy nanotubes potently. Consequently, the developed catalyst presents a superior ORR activity with the half-wave potential of 0.87 V excellent durability with only a 7 mV loss of half-wave potential after 5000 cycles. The catalyst also exhibits superior catalytic performance for OER. When serving as an air electrode in Zn-air batteries, a large power density of 149 mW cm^{-2} and long-term cyclability for over 500 h are realized in ambient air, implying the great potential in practical application.

1. Introduction

The serious energy crisis caused by the burgeoning energy demands of current society and increasingly prominent environmental problems compel us to pursue new energy technologies [1–3]. Among various sustainable energy conversion devices, rechargeable Zn-air batteries have been one of the most promising candidates owing to their high energy density (1086 W h kg^{-1}), improved safety and environmental compatibility [4]. Although encouraging progress has been made on all aspects of this technology, its real commercialization still falls far short of expectations [5]. The oxygen reduction reaction (ORR) and oxygen evolution reaction (OER) at the air cathode play the decisive role in the performance of Zn-air batteries because of the sluggish oxygen electrocatalytic kinetics, which is the primary weakness of Zn-air batteries [6,7]. Besides, it is also challenging to develop high-efficiency catalysts for both ORR and OER. So far, Pt, Ir and RuO_2 are still employed as the most efficient catalysts for ORR or OER [8,9]. However, the high price, limited resource reserve, and insufficient durability hamper the large-scale application of these precious-metal materials in Zn-air battery technologies [10,11]. As a result, development of noble metal free catalysts as alternatives for ORR and OER becomes critically important.

Transition metal-based N-doped porous carbon materials are verified to be the most applicable bifunctional catalysts for ORR and OER by virtue of the distinct chemical properties [12,13]. The precursors

* Corresponding author.
** Corresponding author. MIIT Key Laboratory of Critical Materials Technology for New Energy Conversion and Storage, School of Chemistry and Chemical Engineering, State Key Lab of Urban Water Resource and Environment, Harbin Institute of Technology, Harbin, 150001, China.
*** Corresponding author.
E-mail addresses: leizhao@hit.edu.cn (L. Zhao), wangzhb@hit.edu.cn (Z. Wang), zhwchen@uwaterloo.ca (Z. Chen).

https://doi.org/10.1016/j.nanoen.2020.104592
Received 8 January 2020; Received in revised form 4 February 2020; Accepted 7 February 2020
Available online 12 February 2020

containing transition metals and nitrogen are capable of generating M-N_x (M = Fe, Co, Ni) centers as active sites for efficient oxygen electrocatalysis via the high-temperature pyrolysis [14–16]. Metal-organic frameworks (MOFs) have been deemed as the attractive precursor for ORR and OER with the composition of metal ions and multielement organic ligands, in which different dopant atoms can be introduced as required [17–19]. Besides, the high surface area and porous structure are also promising merits for expedite mass transfer and maximum utilization of active sites [20–22]. But the structural collapse and severe aggregation are inevitable during the pyrolysis process, which significantly limit the catalytic performance [23–25]. Template-assisted method is the most direct and valid means to solve the problem. Several proper substrate materials have been reported to obtain the well-ordered structure, for example, layered-double hydroxides (LDHs) [26], graphene oxide (GO) [27,28], carbon nanotubes (CNTs) [29], MnO_2 nanowires [17] and Te nanowires [30,31]. However, GO-based synthetic strategy normally results in the complex process with a low yield. LDHs and ZnO are applicable substrates to load the MOFs, but their poor electrical conductivity limits the catalytic performance [32]. We have prepared polypyrrole (PPy) nanotubes in the previous work [33], which provides an desirable choice to hold the post of template and nitrogen source because of the special hollow structure and high nitrogen content. Nevertheless, to the bests of our knowledge, there is no report about the assembly of one-dimension nitrogen and cobalt co-doped carbon materials by combining PPy nanotubes and ZIF-67.

Herein, we developed Co nanoparticles embedded in hollow nitrogen doped carbon tubes (Co@hNCTs) to act as highly efficient and durable electrocatalyst for ORR and OER. ZIF-67 nanocrystals are in-situ loaded on the surface of PPy nanotubes which serve as the skeleton and nitrogen source, in which the sodium laurylsulfonate endows PPy nanotubes with functional electronegative surface and enhancing the binding of ZIF-67 nanocrystals with PPy nanotubes. After the calcination process, both ZIF frameworks and PPy nanotubes are carbonized to generate a corn-like Co–N–C catalysts with uniformly dispersed Co nanoparticles embedded within the carbon matrix owing to the potent anchoring effect of the PPy skeleton. The interconnected porous conductive framework supplies a highway for fast electron and ion transfers. Moreover, the catalysts exhibit the hierarchically micro- and mesoporous structure with a large specific surface area, which guarantees a high surface-to-volume ratio and thus significantly increases the exposure of electrocatalytic active sites. Attributed to these merits, the developed catalyst (Co@hNCTs-800) reveals comparable ORR activity with respect to high half-wave potential, 4e reaction pathway, low H_2O_2 yield as well as superior durability and methanol-crossover tolerance compared with commercial Pt/C in alkaline medium. Additionally, it also exhibits a high activity for OER, which is comparable to the RuO_2 benchmark. The Zn-air battery assembled with Co@hNCTs-800 exhibits a high peak current density of 149 mW cm^{-2} and long-term cyclability over 500 h, presenting the possibility in practical application.

2. Experimental section

2.1. Materials

Pyrrole, $FeCl_3$, methyl orange, sodium laurylsulfonate, Co$(NO_3)_2{\cdot}6H_2O$, 2-methylimidazole were all purchased from Shanghai Aladdin Bio-Chem Technology Co. Methanol was purchased from Tianjin Tian Li Bio-Chem Technology Co. All reagents were used directly without further purification.

2.2. Synthesis of polypyrrole (PPy) nanotubes

PPy nanotubes were prepared based on our previous work [33]. In a typical synthesis, 0.1964 g methyl orange was dissolved in 120 mL ultrapure water to form clear orange solution. Then 0.972 g $FeCl_3$ was put into the solution and stirred for 30 min, followed by the injection of 420 μL pyrrole and stirring for 24 h under room temperature. The black product was separated and washed by suction filtration with hot ultrapure water and ethanol. Finally, PPy nanotubes was collected after drying at 80 °C for 5 h in an oven.

2.3. Surface treatment of PPy nanotubes

PPy nanotubes were used after the surface treatment by sodium laurylsulfonate. A certain amount of sodium laurylsulfonate was dissolved in ultrapure water, after which PPy nanotubes and methanol were added into the above solution. The mixture was dispersed by ultrasound for 3 h and then centrifuged with methanol for three times. Afterwards the final product was obtained after dried at 80 °C for 5 h in an oven, which was named S-PPy.

2.4. Synthesis of PPy@ZIF67 and Co@hNCTs-X

100 mg S-PPy and 2 mmol Co$(NO_3)_2{\cdot}6H_2O$ were dispersed in 40 mL methanol by ultrasonic for 3 h. 16 mmol 2-methylimidazole was dissolved in 40 mL methanol to form another clear solution. Then the latter solution was poured into the former solution and stirred for 15 min, afterwards the mixture was kept for 24 h. The product was centrifuged with methanol for three times and dried at 80 °C for 5 h, which is named PPy@ZIF67. At last PPy@ZIF67 was put into a tube furnace and calcined at high temperature for 1 h under Ar, with the temperature rise rate of 3 °C/min. The final product was named Co@hNCTs-X (X is the calcination temperature).

2.5. Synthesis of ZIF-67, PPy/ZIF67, N-hCTs-800, Co,N-NPs-800, and Co,N-CM-800

ZIF-67 was synthesized similarly to the process of PPy@ZIF67 without the use of PPy. PPy/ZIF67 was synthesized similarly to the process of PPy@ZIF67 except that the PPy was not surface treated by sodium laurylsulfonate. N-hCTs-800, Co,N-NPs-800, and Co,N-CM-800 were obtained after the calcination of PPy nanotubes, ZIF-67, or PPy/ZIF67 at 800 °C for 1 h under Ar with the temperature rise rate of 3 °C/min, respectively.

2.6. Physical characterization and electrochemical measurements

X-ray diffraction (XRD), scanning electron microscopy (SEM), transmission electron microscopy (TEM), Scanning transmission electron microscope (STEM), Raman, FT-IR, Nitrogen adsorption−desorption isotherm and X-ray photoelectron spectroscopy (XPS) were used to determine the physical characteristics of the samples. The electrochemical measurements were carried out in a standard three-electrode system. Cyclic voltammetry (CV), staircase voltammetry (SCV) and current-time (i-t) chronoamperometric were performed to investigate the catalytic performance of the catalysts. The detailed parameters are supplied in supporting information.

3. Results and discussion

Co@hNCTs was synthesized by a simple tube-directed templating and following pyrolysis strategy as illustrated in Fig. 1, in which PPy nanotubes were used as structure-directing template for the in-situ growth of ZIF-67 nanocrystals on their surface. PPy nanotubes were firstly prepared using a simple template-assisted method in the presence of methyl orange, which were investigated by SEM and TEM, as shown in Fig. 2a and b. PPy nanotubes exhibit distinct one-dimensional hollow nanotube structure with the diameter ranging from 150 to 300 nm and the length to be several micrometers. FT-IR spectrum is used to determine the chemical structure of PPy nanotubes (Fig. S1). The characteristic peaks at 1548 and 1320 cm^{-1} are assigned to the C═C stretching in polypyrrole rings and the antisymmetric ring-stretching, respectively

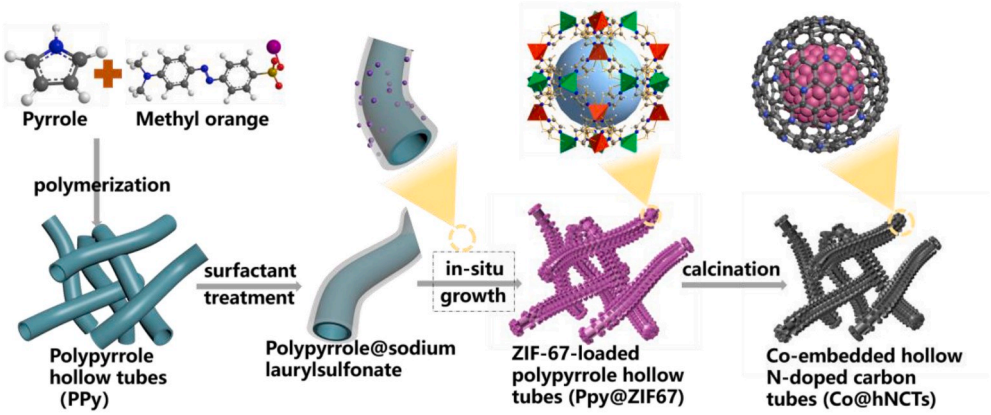

Fig. 1. Schematic illustration for the synthesis of corn-like Co embedded in hollow N-doped carbon tubes (Co@hNCTs) catalysts.

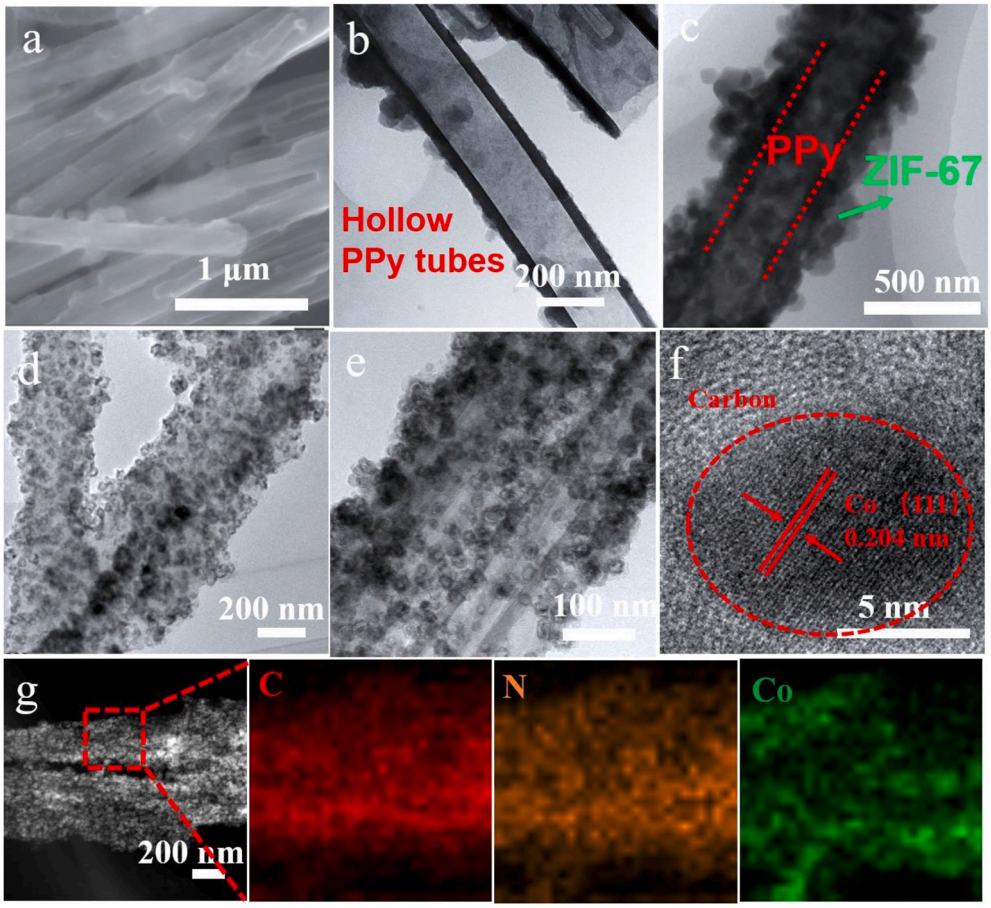

Fig. 2. (a) SEM, (b) TEM images of PPy nanotubes. (c) TEM image of PPy@ZIF67. (d, e) TEM and (f) HR-TEM images of Co@hNCTs-800. (g) STEM image of Co@hNCTs-800 with EDS element mapping for C, N and Co.

[34,35]. The other peaks are located at 1180 cm^{-1} (C–N band), 1036 cm^{-1} (C–H in-plane vibration) and 910 cm^{-1} (C–H out-of-plane deformation), which identifies the presence of polypyrrole [34]. Then sodium laurylsulfonate was chosen to accomplish the surface treatment process, endowing PPy nanotubes with electronegative surface. After removing redundant surfactant and drying, electronegative PPy nanotubes and cobaltous nitrite hexahydrate were dispersed in methanol to form uniform black seriflux, leading to the uniform dispersion of Co^{2+} on the surface of PPy nanotubes under electrostatic force. At the same time, 2-methylimidazole was dissolved in methanol to form the colourless solution, after which the former seriflux was added. The mixture was stirred for 15 min and stood for 24 h without agitating. PPy nanotubes and ZIF-67 nanoparticles assembled into the corn-like structure, in which PPy nanotubes acted as skeleton to in-situ load ZIF-67 nanocrystals, meanwhile, leading to the well-dispersed ZIF-67 nanocrystals with small particle size attributing to the confinement effect. After centrifuging and drying, PPy nanotubes covered with ZIF-67 were gathered as the precursor (PPy@ZIF67). The catalysts were finally obtained after the calcination of PPy@ZIF67 at high temperature, which were marked as Co@hNCTs-X (X means the calcination temperature). ZIF-67 are anchored on the surface of PPy nanotubes and the aggregation is inhibited during the high-temperature treatment, resulting in

corn-like Co–N–C catalysts with highly dispersed Co nanoparticles encapsulated in N-doping porous carbon fibers. The calcination temperature was adjusted to inspect its influence on the final catalysts, such as the morphology, specific surface area, hierarchical pore structure, and the catalytic capability.

The morphologies of different samples were investigated by SEM and TEM in detail. Figs. S2 and 2c show the morphology and microstructure of PPy@ZIF67, proving that ZIF-67 nanocrystals were distributed uniformly on the surface of PPy nanotubes. The surface treatment by anionic surfactant to make PPy nanotubes electronegative is the most pivotal procedure for the in-situ growth of ZIF-67 nanocrystals. Cobalt ion in the solution adsorbed on the surface of surfactant-treated PPy nanotubes owing to electrostatic force, then ZIF-67 nucleated on the surface of PPy, centering on cobalt ion after the addition of the dimethyl imidazole. The particle size of ZIF-67 nanocrystals in PPy@ZIF67 measures to be 80–120 nm, which is much smaller than that of the pristine ZIF-67 (300–400 nm) as shown in Fig. S3. This results from the combined effects of surfactant and confinement effect. On the one hand, the use of surfactant may reduce the size of ZIF-67 to a great extent [36]. Surfactant acts as a capping agent to efficiently control the crystal size due to interactions between dispersed surfactant molecules and the MOF crystals. On the other hand, serried ZIF-67 shoved each other on the surface of PPy nanotubes, exerting potent confinement effect and controlling the growth of ZIF-67 [28]. PPy/ZIF67 was also prepared without surface treatment process as a reference, in which PPy nanotubes and ZIF-67 nanoparticles are disconnected as shown in Fig. S4, indicating the critical role of surfactant as glue to connect ZIF nanocrystals and PPy tubes. Powder XRD pattern of PPy@ZIF67 is accordant with simulated ZIF-67, suggesting the successfully synthesis of ZIF-67 nanocrystals on the surface of the PPy nanotubes (Fig. S5) [37]. After pyrolysis process, the unique structure of the product was retained integrally without breakage (Fig. 2d,e and S6). PPy nanotubes hold the original one-dimension characteristic and ZIF-67-derived fine nanoparticles anchor firmly on PPy nanotubes. Meanwhile, pristine ZIF-67 was also subject to the high-temperature calcination as a reference to dissect the effect of PPy skeleton on the structure of product. Co,N-NPs-800 proves to be fragmentized and aggregated particles according to the SEM images in Fig. S7, leading to the decrease of the accessible active sites. This comparison of Fig. 2e and S7 directly demonstrates the critical role of the PPy template. PPy template not only serves as carbon and nitrogen source, but also plays the role of skeleton to connect and anchor ZIF-67 on its surface to reduce the particle size and hold back the aggregation of Co nanoparticles. Both of the two effects lead to the isolation and confinement of Co nanoparticles on the surface of PPy-derived carbon tubes, thus improving the catalytic capability of the catalysts. High-resolution TEM (HR-TEM) measurement was carried out to determine the fine structure of the catalyst (Fig. 2f). Distinct crystal lattice is exposed in the image, whose distance is 0.204 nm, assignable to d-space of Co (111) plane. And cobalt nanoparticles are encompassed within carbon shell, which is conducive to suppressing the aggregation of Co particles thus gaining the high catalytic stability in the operating conditions [38,39]. STEM measurement was carried out to further identify the exquisite structure of the catalyst and element mapping images indicate the homogeneous distribution of C, N and Co in carbon matrix (Fig. 2g). It is recognized that the calcination temperature has a significant influence on the microstructure and physical characteristics of the products. Fig. S8 shows the TEM images of the products calcined at different temperatures, which exhibits similar morphology except the increase of the particles size under raised temperature. The gradually varied particle size indicates the serious aggregation of Co nanoparticles under high temperature, which is consistent with the SEM images in Fig. S9.

The chemical composition and crystallographic structure of the as-prepared catalysts was determined by XRD. As shown in Fig. S10, Co@hNCTs-800 presents a broad peak at 26° corresponding to (002) plane of carbon, while the other weak peaks are ascribed to cobalt (PDF#89–4307). Surface area and pore structure are the significant factors to affect the performance of the catalysts, which were investigated by the nitrogen adsorption-desorption measurement. As shown in Fig. 3a, Co@hNCTs-800 reveals comprehensive characteristic of type I and IV isotherm, implying the hierarchical porous structure in the catalysts. Quick N_2 uptake at low pressure suggests the existence of micropores, which basically resulted from ZIF-67 derived nanoparticles [27]. Besides, hysteresis loop at the high P/P_0 indicates the presence of mesopores are mainly from the hollow one-dimension nanotubes that are derived from the PPy skeleton. The other catalysts exhibit similar nitrogen adsorption-desorption isotherms curves along with the change of pyrolysis temperature, meaning the co-existence of micropores and mesopores in all samples. The specific surface area obtained by Brunauer–Emmett–Teller (BET) method are 271, 307, 246 and 155 $m^2\ g^{-1}$ for Co@hNCTs-X with X equivalent to 700, 800, 900 and 1000, respectively. The decrease of the BET surface area may be correlative to the aggregation of cobalt and the collapse of pore structure as pyrolysis temperature increase [40,41]. Higher specific surface area is favorable for the exposure of active sites as much as possible, which is advantageous for the improvement of catalytic performance [42]. The catalysts display hierarchical porous structure with the pore size mainly arranging from 0.6 to 28 nm, according to the pore size distributions shown in Fig. 3b. Hierarchical porous structure endows the catalysts with strong ability to be sufficiently infused by electrolyte, decreasing the diffusion resistance and promoting the mass transfer rate, which is highly effective for the oxygen electrocatalytic reactions [43]. Raman spectra of Co@hNCTs-800 demonstrates two peaks at around 1340 and 1590 cm^{-1}, pointing to D band and G band of carbon (Fig. 3c). D band and G band are related to the disordered sp^3 hybridization carbon and graphitic sp^2 carbon, respectively, where the value of I_D/I_G characteristically represent the degree of defect in graphite plane [44]. As calcination temperature rising from 700 to 1000 °C, the values of I_D/I_G calculate to be 1.15, 1.13, 1.12 and 1.06, suggesting that higher temperature is devoted to the ordered arrangement of graphite lattice and reduced defect. The high I_D/I_G ratio confirms the existence of numerous structural defects, which contributes to the enhancement of ORR catalytic capability [45].

XPS was carried out to investigate the element composition and chemical structure of the as-prepared catalysts. C, N, O and Co elements present in the catalysts in the light of the XPS survey spectra in Fig. S11, where the content of the four elements is summarized in Table S1. High-resolution C 1s spectra (Fig. 3d) are classified into three different peaks, which are C–C (284.6 eV), C–N (285.4 eV) and C–O (286.9 eV), respectively [46–48]. Moreover, Co incorporation is beneficial to the transformation of carbon framework to highly graphitic structure under pyrolysis process [49]. High-resolution Co $2p_{3/2}$ XPS spectra reveals the presence of Co (778 eV), Co^{3+} (779.3 eV), Co^{2+}(780.8 eV), Co-N_x (781.8 eV) and shakeup satellite (Fig. 3e) [24,37,50]. For the N 1s, three different kinds of N can be observed in Fig. 3f, corresponding to pyridinic N (398.7 eV), pyrrole N (400.3 eV) and graphite N (401.5 eV) [50,51]. Apparent decrease of total N can be perceived according to Table S2, which are 5.68%, 5.47%, 2.93%, 1.39% for Co@hNCTs-X (700, 800, 900 and 1000). Besides, pyridinic N and pyrrole N decrease with pyrolysis temperature rising, on the contrary, graphite N increases. As reported in literatures, pyridinic N and pyrrole N are labile at high temperature and converted into thermostable graphite N, bringing about the augmentation of graphite N content [43]. Up to now, the authentic effect of different types of N in ORR is still a controversial debate, which is ponderable but tough to be achieved. One of the conclusive consequences to be accepted is that pyridinic N and graphite N play the most important role in facilitating the catalytic reaction [52]. It is not difficult to find that pyridinic N and graphite N occupy the dominant proportion in Co@hNCTs-800, which is one of the principal elements for the excellent performance.

The catalytic performance of the catalysts towards oxygen reduction was firstly determined by cyclic voltammetry (CV) experiment in N_2- or

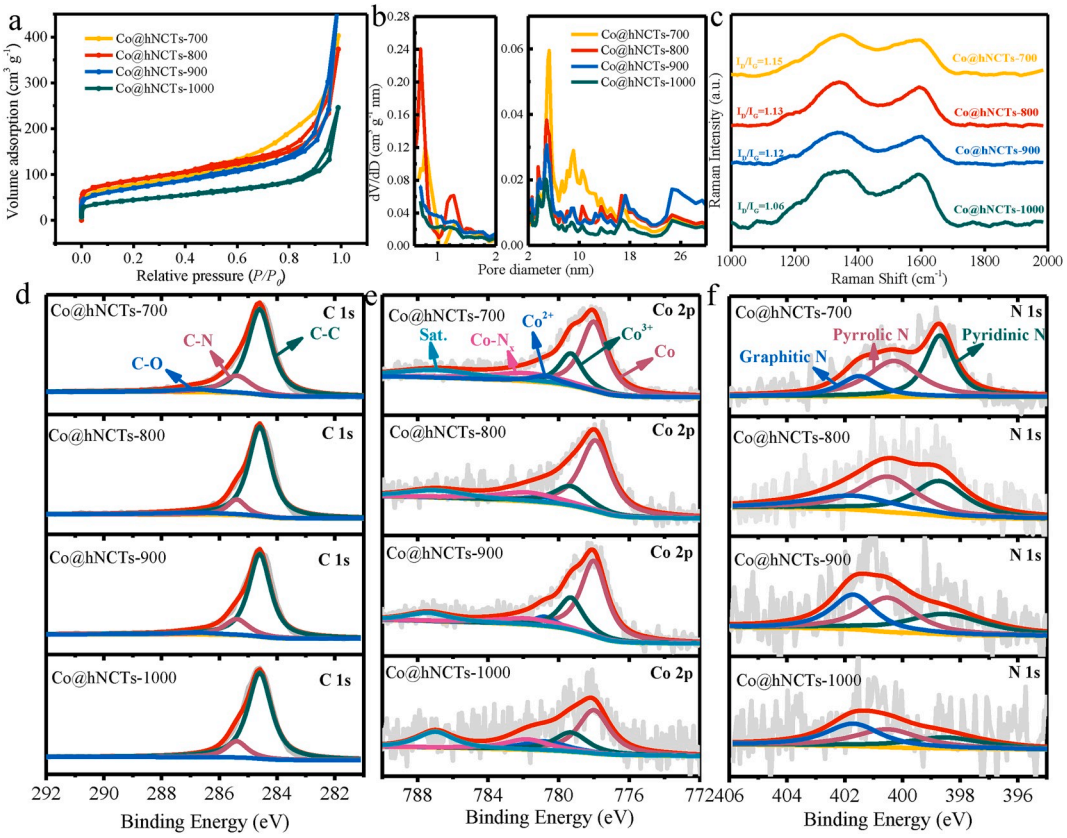

Fig. 3. (a) N_2 adsorption-desorption isotherms curves, (b) pore size distributions, (c) Raman spectra and high-resolution (d) C 1s, (e) Co 2p and (f) N 1s XPS spectrum of the samples with different pyrolysis temperatures.

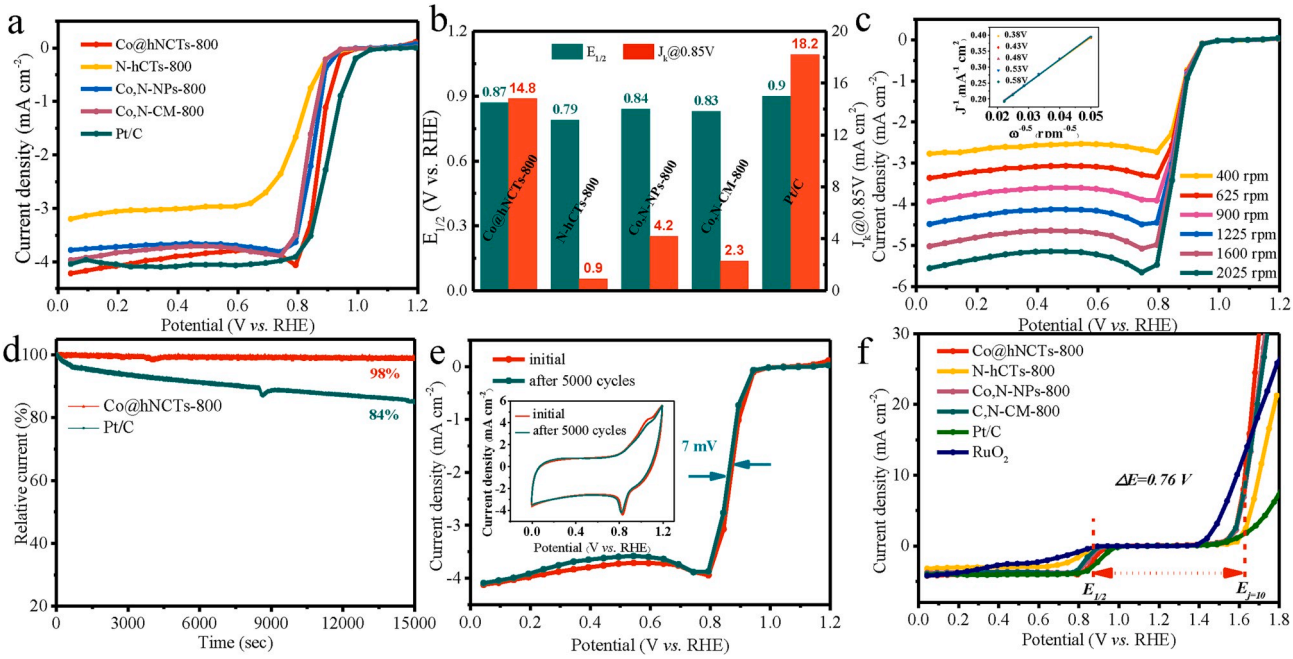

Fig. 4. (a) SCV curves of different samples as reference obtained in O_2-saturated 0.1 mol L^{-1} KOH electrolyte with a rotating speed of 900 rpm. (b) Comparison of half-wave potential and J_k@0.85 V for different catalysts. (c) SCV curves of Co@hNCTs-800 at different rotating speeds and corresponding K-L plots at different potentials (insert). (d) Chronoamperometric responses of Co@hNCTs-800 and Pt/C in O_2-saturated 0.1 mol L^{-1} KOH electrolyte at a rotating speed of 900 rpm. (e) Long-term durability test for Co@hNCTs-800 by recording the SCV and CV (insert) curves after 5000 cycles from 0.6 V to 1 V. (f) SCV curves of different catalysts for both ORR and OER in O_2-saturated 0.1 M KOH at 900 rpm.

O_2-saturated 0.1 mol L^{-1} KOH electrolyte. As can be seen in Fig. S12, Co@hNCTs-800 shows unnoteworthy capacity curve when subject to N_2-saturated electrolyte. In contrast, a pronounced cathodic redox peak located at 0.82 V (vs. RHE) was gained after the saturation of O_2, meaning its capability for electrocatalytic reduction of oxygen. Additionally, Co@hNCTs-800 exhibits more positive oxygen reduction peak than other catalysts calcined at other temperatures, implying the best catalytic ability of Co@hNCTs-800 among the four catalysts (Fig. S13). The same conclusion can be obtained according to the staircase voltammetry (SCV) obtained in O_2-saturated 0.1 mol L^{-1} KOH at 900 rpm (Fig. S14). It can be observed that Co@hNCTs-800 affords stronger catalytic ability towards ORR in accordance with more positive onset and half-wave potential. Co@hNCTs-800 has the largest specific surface area, abundant defects, high content of active pyridinic N and graphite N compared with other catalysts. Besides, serious aggregation of cobalt nanoparticles occurred at extremely high calcination temperature, which affects the exposure of active sites to a great degree. All of the factors destine that Co@hNCTs-800 delivers the best catalytic performance towards ORR. In order to investigate the exact function of the particular one-dimension corn-like structure, variety of samples were synthesized as reference and commercial Pt/C is selected to serve as the benchmark to appraise the oxygen reduction performance of the as-prepared samples (Fig. 4a). Notably, Co@hNCTs-800 presents an excellent half-wave potential of 0.87 V, which is comparable to commercial Pt/C of 0.90 V. Moreover, the catalysts obtained from pure PPy shows much poorer catalytic performance than Co@hNCTs-800 in terms of half-wave potential of 0.79 V and low limiting current density, confirming the undisputed status of Co for the catalysis of oxygen reduction. The half-wave potentials of Co,N-NPs-800 (derived from ZIF-67) and Co, N-CM-800 (derived from PPy/ZIF67) are measured to be 0.84 V and 0.83 V, close to each other. The approximate ORR performance of Co,N-NPs-800 and Co,N-CM-800 indicates that it is invalid to toughly add PPy to the original system, even causing the decline of the catalytic capability. On the contrary, the in-situ combination of PPy nanotubes and ZIF-67 nanoparticles endows the catalysts with unique corn-like structure, resulting in more dispersive active sites and shorter mass transfer distance to promote the ORR activity. Moreover, the kinetic current density (J_k@0.85 V) of Co@hNCTs-800 is calculated to be 14.8 mA cm^2, which is 16.4, 3.5 and 6.4 times the value of N-hCTs-800, Co,N-NPs-800 and Co,N-CM-800, respectively (Fig. 4b). As a result, Co@hNCTs-800 is deemed to be one of the best Co–N–C catalysts for ORR compared with the as-reported catalysts in literatures (Table S3).

Fig. 4c shows the SCV curves of Co@hNCTs-800 obtained at different rotating speeds and corresponding K-L plots at different potentials (insert). The electron transfer number (n) is checked to be around 3.9 according to Koutecky-Levich equation, suggesting the approximate 4 e pathway in the reaction process and providing another convincing evidence for the splendid ORR activity. Rotating ring-disk electrode (RRDE) test was further carried out to examine the kinetics of the oxygen reduction process (Fig. S15). The n value of Co@hNCTs-800 is 3.85–3.88 calculated by the results of RRDE test, which is anastomotic to the above consequence, verifying the superb catalytic performance of Co@hNCTs-800. The H_2O_2 yield is never beyond 8.0% in the whole potential range, further signifying the direct 4 e^- ORR process. It can also be observed that Co@hNCTs-800 shows close electron transfer number and H_2O_2 yield to commercial Pt/C, which renders it the competitive catalytic capability to commercial Pt/C.

The durability of Co@hNCTs-800 and Pt/C was firstly examined by current-time (i-t) chronoamperometric test shown in Fig. 4d. After 15000 s continuous test, only a 2% loss of current density is detected for Co@hNCTs-800, signifying the preeminent durability in reaction. As a reference, Pt/C exhibits an 84% retention after the same test, which is put down to the disintegration and aggregation of the Pt atoms during the process. The reason for the preeminent durability of Co@hNCTs-800 may be the anchoring of ZIF-67 on PPy nanotubes in the original step, which caused the firmly combination of Co and the one-dimension skeleton, so as to restrict the migration and the aggregation of cobalt nanoparticles. What's more, long-term stability of the samples is inspected through continuous 5000 cycles in O_2-saturated KOH from 0.6 V to 1 V. Co@hNCTs-800 presents almost unchanged CV and SCV curves before and after the test (Fig. 4e), while commercial Pt/C has a 37 mV shift of half-wave potential (Fig. S16), further verifying the much better stability of Co@hNCTs-800 than commercial Pt/C. Fig. S17 exhibits SEM and TEM images of Co@hNCTs-800 after the long-term stability test. It can be observed clearly that the Co@hNCTs-800 still retained corn-like structure without obvious damage after the long-term durability test. Besides, the size of cobalt particles derived from ZIF-67 has increased slightly. The unique structure impedes the collapse of the ZIF-67-derived nanoparticles and the strong anchoring effect between the Co nanoparticles and carbon tubes can minimize agglomeration of metal nanoparticles, which was positive for the durability of the catalysts. The insight for methanol tolerance is operated by adding methanol to the O_2-saturated KOH during current-time chronoamperometric test (Fig. S18). Co@hNCTs-800 is hardly impacted by the introduction of methanol, yet commercial Pt/C shows seriously impressionable peculiarity to methanol, resulting in rapid decline of current density. Similar consequence can be obtained from the SCV curves gained in O_2-saturated KOH electrolyte with and without methanol (Fig. S19). Negligible variation is observed for the SCV curves of Co@hNCTs-800 after the addition of methanol, whereas distinct methanol oxidation peak occurs for Pt/C. Series of measurements render the Co@hNCTs-800 catalysts remarkable tolerance to methanol crossover, implying the better catalytic selectivity than Pt/C. To further detect the bifunctional electrocatalytic performance of the catalysts for ORR and OER, the potential difference between OER and ORR ($\triangle E = E_{j=10}\text{-}E_{1/2}$) is calculated as evaluation standard. As can be seen in Fig. 4f, the potential at the current density of 10 mA cm^{-2} for Co@hNCTs-800 is 1.63 V, which is comparable to RuO_2 (1.59 V) and slightly prevail over those of N-hCTs-800 (1.70 V), Co,N-NPs-800 (1.64 V), and Co,N-CMs-800 (1.64 V). Besides, it is obvious that Co@hNCTs-800 possesses the smallest $\triangle E$ of 0.76 V among all the four catalysts, suggesting the best catalysts for reversible oxygen electrode.

A liquid primary Zn-air battery was assembled to assess the practical application of Co@hNCTs-800 catalysts, in which Co@hNCTs-800 serves as the catalyst for air cathode and Zn plate serves as anode, which was illustrated in Fig. 5a. Another two Zn-air batteries were constructed as a reference using commercial Pt/C and Pt/C–RuO_2 as catalysts under the same condition. As can be seen in Fig. S20a, the open-circuit is determined to be 1.45 V for the Zn-air battery with Co@hNCTs-800 catalysts. To further determine the feasibility of the batteries in the real environment, two Zn-air batteries were connected in series to drive the 'HIT' pattern formed by 40 LEDs (5 mm, 2 V), as shown in Fig. 5b. Fig. 5c shows the charge and discharge polarization curves of the rechargeable Zn-air batteries, in which the battery with Co@hNCTs-800 exhibits similar charge performance but better discharge performance than the other with Pt/C and RuO_2. According to discharge polarization and power density curves in Fig. 5d, the Zn-air batteries with Co@hNCTs-800 and commercial Pt/C catalysts display the maximum power density of 149 and 120 mW cm^{-2}, respectively, indicating the superior ORR performance of Co@hNCTs-800 to commercial Pt/C. Galvanostatically discharge test was operated at 10 mA cm^{-2} to examine the specific capacity of the batteries, which is calculated according to the mass loss of Zn. The battery based on Co@hNCTs-800 catalyst exhibited 746 mAh g_{Zn}^{-1}, suggesting the more remarkable performance of the Co@hNCTs-800-based Zn-air battery (Fig. S20b). Further test was operated to investigate the charge and discharge cycle performance by galvanostatically charge and discharge tests at 5 mA cm^{-2} (10 min per cycle), as can be seen in Fig. 5e. The Zn-air battery with Co@hNCTs-800-based air cathode shows the charge/discharge gap of 0.82 V for the first cycle, suggesting remarkable OER and ORR performance of the catalysts. Fig. 5e shows the cycling performance of the two batteries, in which Co@hNCTs-800-based battery still exhibits a

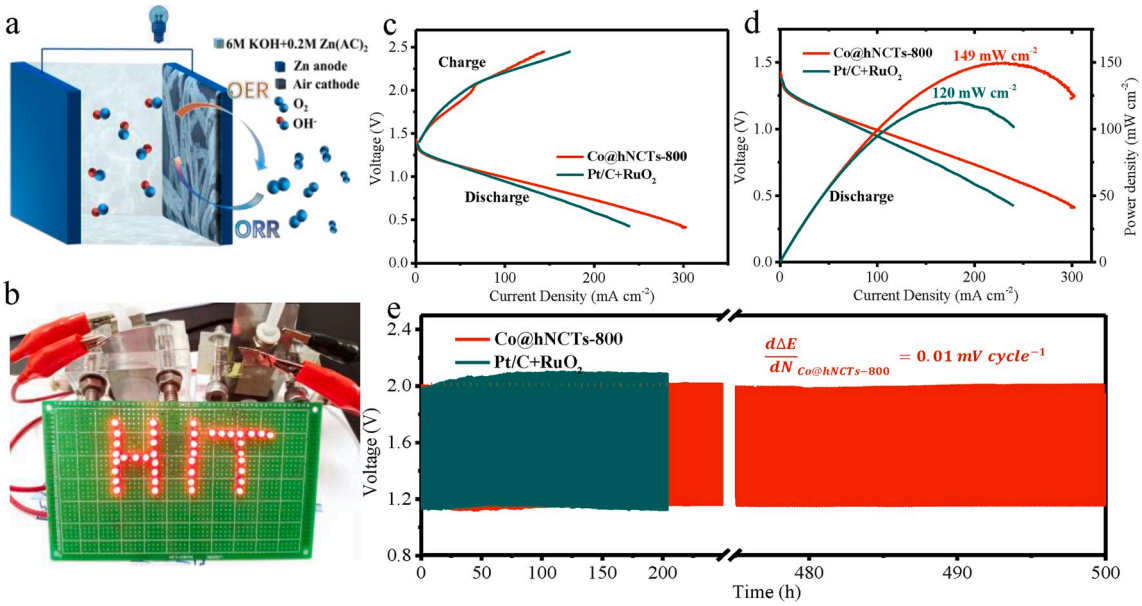

Fig. 5. (a) Schematic illustration of the Zn-air battery. (b) Photograph of a 'HIT' pattern formed by 40 LEDs driven by two Zn-air batteries. (c) Charge and discharge polarization curves, (d) discharge polarization and power density curves of the Zn-air batteries with different catalysts. (e) Galvanostatic cycling performance of the Zn-air batteries with different catalysts at a current density of 5 mA cm^{-2} (10 min per cycle).

narrow charge/discharge gap of 0.85 V after 500 h test, revealing the excellent long-term cyclability. The decaying rate of the battery is calculated to be only 0.01 mV per cycle, further implying the remarkable stability of the catalyst. By contrast, the Pt/C + RuO_2-based Zn-air battery shows quick performance degradation during the test.

So far, there is no report about the in-situ combination of PPy nanotubes and ZIF-67 nanoparticles as precursor to prepare highly effective catalyst for both ORR and OER. The excellent catalytic activity of Co@hNCTs-800 is related to the unique corn-like structure of cobalt and nitrogen co-doped carbon nanotubes. Firstly, PPy nanotubes play the role of one-dimension template and nitrogen source to in-situ load ZIF-67 particles on their surface, leading to corn-like Co,N-doped hollow carbon tubes after pyrolysis process, which was beneficial for the expedite mass and electron transfer. The combined action of surfactant and PPy nanotubes is the crucial factor for the synthesis of the special-structure catalysts. Secondly, the surfactant modified PPy nanotubes serve as the skeleton to promote the dispersion of ZIF-67 and prevent the aggregation of cobalt nanoparticles under calcination. This not only provides ample accessibility for reacting species to active sites, but also guarantees a remarkable durability of the catalysts. In addition, micropores and mesopores coexist in the catalysts, constituting the unique hierarchical porous structure to fortify the efficient exposure of active sites and rapid mass transfer. The synergistic integration of all the aforesaid peculiarities makes Co@hNCTs-800 to be one of the best oxygen electrocatalysts with comparable activity, higher stability and better catalytic selectivity relative to commercial Pt/C and RuO_2.

4. Conclusions

In summary, we elaborately developed a unique and facile tube-directed templating strategy for the fabrication of corn-like Co, N-doped hollow carbon tubes (Co@hNCTs) catalysts with hierarchical pore structure. PPy nanotubes played the roles of conductive skeleton to in-situ load ZIF-67 on their surface, thus driving highly dispersive cobalt nanoparticles to anchor on hollow carbon nanotubes with micro/mesopores co-existence system. The integration of the unique structure and high specific surface area renders the synthesized catalysts remarkable catalytic activity toward ORR, which shows a half-wave potential of 0.87 V in the alkaline medium. The negligible variation in durability and methanol tolerance tests also suggests their better stability and catalytic selectivity than commercial Pt/C. In addition, the Zn-air battery assembled with Co@hNCTs-800 exhibits a large peak current density of 149 mW cm^{-2} and superior cycling durability. The present work offers a feasible strategy to design and prepare hierarchically structural materials as highly effective catalysts in the field of energy storage and conversion.

Declaration of competing interest

The authors declare that they have no known competing financial interests or personal relationships that could have appeared to influence the work reported in this paper.

Acknowledge

We acknowledge the financial support of National Natural Science Foundation of China (Grant No. 21673064, 51802059, 21905070and U1909213), China Postdoctoral Science Foundation (Grant No. 2018M631938, 2018T110307 and 2017M621284), Heilongjiang Postdoctoral Fund (LBH-Z17074 and LBH-Z18066), Fundamental Research Funds for the Central Universities (Grant No. HIT. NSRIF. 2019040 and 2019041), the Natural Sciences and Engineering Research Council of Canada (NSERC), University of Waterloo, and Waterloo Institute for Nanotechnology, University of Waterloo.

Appendix A. Supplementary data

Supplementary data to this article can be found online at https://doi.org/10.1016/j.nanoen.2020.104592.

References

[1] J. Lu, T. Wu, K. Amine, State-of-the-art characterization techniques for advanced lithium-ion batteries, Nat. Energy 2 (2017) 17011.
[2] C. Xuan, B. Hou, W. Xia, Z. Peng, T. Shen, H.L. Xin, G. Zhang, D. Wang, From a ZIF-8 polyhedron to three-dimensional nitrogen doped hierarchical porous carbon: an efficient electrocatalyst for the oxygen reduction reaction, J. Mater. Chem. A 6 (2018) 10731–10739.

[3] J. Zhang, G. Jiang, T. Cumberland, P. Xu, Y. Wu, S. Delaat, A. Yu, Z. Chen, A highly sensitive breathable fuel cell gas sensor with nanocomposite solid electrolyte, InfoMat 1 (2019) 234–241.
[4] Y. Jiang, Y.-P. Deng, J. Fu, D.U. Lee, R. Liang, Z.P. Cano, Y. Liu, Z. Bai, S. Hwang, L. Yang, D. Su, W. Chu, Z. Chen, Interpenetrating triphase cobalt-based nanocomposites as efficient bifunctional oxygen electrocatalysts for long-lasting rechargeable Zn-air batteries, Adv. Energy Mater. 8 (2018), 1702900.
[5] X. Liu, M. Park, M.G. Kim, S. Gupta, G. Wu, J. Cho, Integrating NiCo alloys with their oxides as efficient bifunctional cathode catalysts for rechargeable zinc–air batteries, Angew. Chem. Int. Ed. 54 (2015) 9654–9658.
[6] J.-J. Cai, Q.-Y. Zhou, B. Liu, X.-F. Gong, Y.-L. Zhang, K. Goh, D.-M. Gu, L. Zhao, X.-L. Sui, Z.-B. Wang, A sponge-templated sandwich-like cobalt-embedded nitrogen-doped carbon polyhedron/graphene composite as a highly efficient catalyst for Zn–air batteries, Nanoscale 12 (2020) 973–982.
[7] R. Cao, J.-S. Lee, M. Liu, J. Cho, Recent progress in non-precious catalysts for metal-air batteries, Adv. Energy Mater. 2 (2012) 816–829.
[8] X. Liu, M. Park, M.G. Kim, S. Gupta, X. Wang, G. Wu, J. Cho, High-performance non-spinel cobalt–manganese mixed oxide-based bifunctional electrocatalysts for rechargeable zinc–air batteries, Nano Energy 20 (2016) 315–325.
[9] Z. Liu, Z. Zhao, Y. Wang, S. Dou, D. Yan, D. Liu, Z. Xia, S. Wang, In situ exfoliated, edge-rich, oxygen-functionalized graphene from carbon fibers for oxygen electrocatalysis, Adv. Mater. 29 (2017), 1606207.
[10] Z. Wang, H. Jin, T. Meng, K. Liao, W. Meng, J. Yang, D. He, Y. Xiong, S. Mu, Fe, Cu-coordinated ZIF-derived carbon framework for efficient oxygen reduction reaction and zinc–air batteries, Adv. Funct. Mater. 28 (2018), 1802596.
[11] C. Tang, B. Wang, H.-F. Wang, Q. Zhang, Defect engineering toward atomic Co–nx–C in hierarchical graphene for rechargeable flexible solid Zn-air batteries, Adv. Mater. 29 (2017), 1703185.
[12] R. Cao, R. Thapa, H. Kim, X. Xu, M.G. Kim, Q. Li, N. Park, M. Liu, J. Cho, Promotion of oxygen reduction by a bio-inspired tethered iron phthalocyanine carbon nanotube-based catalyst, Nat. Commun. 4 (2013) 2076.
[13] L. Chen, Y. Zhang, X. Liu, L. Long, S. Wang, X. Xu, M. Liu, W. Yang, J. Jia, Bifunctional oxygen electrodes of homogeneous Co4N nanocrystals@N-doped carbon hybrids for rechargeable Zn-air batteries, Carbon 151 (2019) 10–17.
[14] X. Chen, Z. Yan, M. Yu, H. Sun, F. Liu, Q. Zhang, F. Cheng, J. Chen, Spinel oxide nanoparticles embedded in nitrogen-doped carbon nanofibers as a robust and self-standing bifunctional oxygen cathode for Zn–air batteries, J. Mater. Chem. A 7 (2019) 24868–24876.
[15] J. Luo, K. Wang, X. Hua, W. Wang, J. Li, S. Zhang, S. Chen, Pyridinic-N protected synthesis of 3D nitrogen-doped porous carbon with increased mesoporous defects for oxygen reduction, Small 15 (2019), e1805325.
[16] S. Dou, X. Li, L. Tao, J. Huo, S. Wang, Cobalt nanoparticle-embedded carbon nanotube/porous carbon hybrid derived from MOF-encapsulated Co3O4 for oxygen electrocatalysis, Chem. Commun. 52 (2016) 9727–9730.
[17] H. Luo, B. Wang, T. Liu, F. Jin, R. Liu, C. Xu, C. Wang, K. Ji, Y. Zhou, D. Wang, S. Dou, Hierarchical design of hollow Co-Ni LDH nanocages strung by MnO2 nanowire with enhanced pseudocapacitive properties, Energy Storage Mater 19 (2019) 370–378.
[18] L. Tao, C.-Y. Lin, S. Dou, S. Feng, D. Chen, D. Liu, J. Huo, Z. Xia, S. Wang, Creating coordinatively unsaturated metal sites in metal-organic-frameworks as efficient electrocatalysts for the oxygen evolution reaction: insights into the active centers, Nano Energy 41 (2017) 417–425.
[19] B.Y. Xia, Y. Yan, N. Li, H.B. Wu, X.W. Lou, X. Wang, A metal–organic framework-derived bifunctional oxygen electrocatalyst, Nat. Energy 1 (2016) 15006.
[20] H. Jiang, Y. Liu, W. Li, J. Li, Co nanoparticles confined in 3D nitrogen-doped porous carbon foams as bifunctional electrocatalysts for long-life rechargeable Zn-air batteries, Small 14 (2018), e1703739.
[21] Y. Wang, L. Tao, Z. Xiao, R. Chen, Z. Jiang, S. Wang, 3D carbon electrocatalysts in situ constructed by defect-rich nanosheets and polyhedrons from NaCl-sealed zeolitic imidazolate frameworks, Adv. Funct. Mater. 28 (2018), 1705356.
[22] Z. Wang, Y. Lu, Y. Yan, T.Y.P. Larissa, X. Zhang, D. Wuu, H. Zhang, Y. Yang, X. Wang, Core-shell carbon materials derived from metal-organic frameworks as an efficient oxygen bifunctional electrocatalyst, Nano Energy 30 (2016) 368–378.
[23] Y.-N. Chen, Y. Guo, H. Cui, Z. Xie, X. Zhang, J. Wei, Z. Zhou, Bifunctional electrocatalysts of MOF-derived Co–N/C on bamboo-like MnO nanowires for high-performance liquid- and solid-state Zn–air batteries, J. Mater. Chem. A 6 (2018) 9716–9722.
[24] Z. Liang, C. Zhang, H. Yuan, W. Zhang, H. Zheng, R. Cao, PVP-assisted transformation of a metal-organic framework into Co-embedded N-enriched meso/microporous carbon materials as bifunctional electrocatalysts, Chem. Commun. 54 (2018) 7519–7522.
[25] Y. He, S. Hwang, D.A. Cullen, M.A. Uddin, L. Langhorst, B. Li, S. Karakalos, A. J. Kropf, E.C. Wegener, J. Sokolowski, M. Chen, D. Myers, D. Su, K.L. More, G. Wang, S. Litster, G. Wu, Highly active atomically dispersed CoN4 fuel cell cathode catalysts derived from surfactant-assisted MOFs: carbon-shell confinement strategy, Energy Environ. Sci. 12 (2019) 250–260.
[26] Z. Li, M. Shao, L. Zhou, R. Zhang, C. Zhang, M. Wei, D.G. Evans, X. Duan, Directed growth of metal-organic frameworks and their derived carbon-based network for efficient electrocatalytic oxygen reduction, Adv. Mater. 28 (2016) 2337–2344.
[27] K. Chen, Z. Sun, R. Fang, Y. Shi, H.-M. Cheng, F. Li, Metal-organic frameworks (MOFs)-Derived nitrogen-doped porous carbon anchored on graphene with multifunctional effects for lithium-sulfur batteries, Adv. Funct. Mater. 28 (2018), 1707592.
[28] W. Xia, C. Qu, Z. Liang, B. Zhao, S. Dai, B. Qiu, Y. Jiao, Q. Zhang, X. Huang, W. Guo, D. Dang, R. Zou, D. Xia, Q. Xu, M. Liu, High-performance energy storage and conversion materials derived from a single metal-organic framework/graphene aerogel composite, Nano Lett. 17 (2017) 2788–2795.
[29] L. Wan, E. Shamsaei, C.D. Easton, D. Yu, Y. Liang, X. Chen, Z. Abbasi, A. Akbari, X. Zhang, H. Wang, ZIF-8 derived nitrogen-doped porous carbon/carbon nanotube composite for high-performance supercapacitor, Carbon 121 (2017) 330–336.
[30] S.H. Ahn, M.J. Klein, A. Manthiram, 1D Co- and N-doped hierarchically porous carbon nanotubes derived from bimetallic metal organic framework for efficient oxygen and tri-iodide reduction reactions, Adv. Energy Mater. 7 (2017), 1601979.
[31] W. Zhang, Z.-Y. Wu, H.-L. Jiang, S.-H. Yu, Nanowire-directed templating synthesis of metal–organic framework nanofibers and their derived porous doped carbon nanofibers for enhanced electrocatalysis, J. Am. Chem. Soc. 136 (2014) 14385–14388.
[32] Q. Bai, F.C. Shen, S.L. Li, J. Liu, L.Z. Dong, Z.M. Wang, Y.Q. Lan, Cobalt@Nitrogen-Doped porous carbon fiber derived from the electrospun fiber of bimetal–organic framework for highly active oxygen reduction, Small Methods 2 (2018), 1800049.
[33] L.-M. Zhang, X.-L. Sui, L. Zhao, J.-J. Zhang, D.-M. Gu, Z.-B. Wang, Nitrogen-doped carbon nanotubes for high-performance platinum-based catalysts in methanol oxidation reaction, Carbon 108 (2016) 561–567.
[34] J. Liu, M. Gu, L. Ouyang, H. Wang, L. Yang, M. Zhu, Sandwich-like SnS/polypyrrole ultrathin nanosheets as high-performance anode materials for Li-ion batteries, ACS Appl. Mater. Interfaces 8 (2016) 8502–8510.
[35] Q. Lai, J. Zhu, Y. Zhao, Y. Liang, J. He, J. Chen, MOF-based metal-doping-induced synthesis of hierarchical porous CuN/C oxygen reduction electrocatalysts for Zn-air batteries, Small 13 (2017), 1700740.
[36] Y. Pan, D. Heryadi, F. Zhou, L. Zhao, G. Lestari, H. Su, Z. Lai, Tuning the crystal morphology and size of zeolitic imidazolate framework-8 in aqueous solution by surfactants, CrystEngComm 13 (2011) 6937–6940.
[37] Y.Z. Chen, C. Wang, Z.Y. Wu, Y. Xiong, Q. Xu, S.H. Yu, H.L. Jiang, From bimetallic metal-organic framework to porous carbon: high surface area and multicomponent active dopants for excellent electrocatalysis, Adv. Mater. 27 (2015) 5010–5016.
[38] W. Zhang, X. Jiang, X. Wang, Y.V. Kaneti, Y. Chen, J. Liu, J.S. Jiang, Y. Yamauchi, M. Hu, Spontaneous weaving of graphitic carbon networks synthesized by pyrolysis of ZIF-67 crystals, Angew. Chem. Int. Ed. 56 (2017) 8435–8440.
[39] S.H. Ahn, A. Manthiram, Cobalt phosphide coupled with heteroatom-doped nanocarbon hybrid electroctalysts for efficient, long-life rechargeable zinc-air batteries, Small 13 (2017), 1702068.
[40] L.-Y. Zhang, M.-R. Wang, Y.-Q. Lai, X.-Y. Li, Nitrogen-doped microporous carbon: an efficient oxygen reduction catalyst for Zn-air batteries, J. Power Sources 359 (2017) 71–79.
[41] B. Chen, X. He, F. Yin, H. Wang, D.-J. Liu, R. Shi, J. Chen, H. Yin, MO-Co@N-Doped carbon (M = Zn or Co): vital roles of inactive Zn and highly efficient activity toward oxygen reduction/evolution reactions for rechargeable Zn-air battery, Adv. Funct. Mater. (2017), 1700795.
[42] Y. Zan, Z. Zhang, H. Liu, M. Dou, F. Wang, Nitrogen and phosphorus co-doped hierarchically porous carbons derived from cattle bones as efficient metal-free electrocatalysts for the oxygen reduction reaction, J. Mater. Chem. A 5 (2017) 24329–24334.
[43] L. Zhao, X.-L. Sui, Q.-Y. Zhou, J.-Z. Li, J.-J. Zhang, G.-S. Huang, Z.-B. Wang, 1D N-doped hierarchically porous hollow carbon tubes derived from a supramolecular template as metal-free electrocatalysts for a highly efficient oxygen reduction reaction, J. Mater. Chem. A 6 (2018) 6212–6219.
[44] T. Zhou, Y. Zhou, R. Ma, Z. Zhou, G. Liu, Q. Liu, Y. Zhu, J. Wang, Nitrogen-doped hollow mesoporous carbon spheres as a highly active and stable metal-free electrocatalyst for oxygen reduction, Carbon 114 (2017) 177–186.
[45] S. Han, X. Hu, J. Wang, X. Fang, Y. Zhu, Novel route to Fe-based cathode as an efficient bifunctional catalysts for rechargeable Zn-air battery, Adv. Energy Mater. 8 (2018), 1800955.
[46] Q. Guo, Y. Ma, T. Chen, Q. Xia, M. Yang, H. Xia, Y. Yu, Cobalt sulfide quantum dot embedded N/S-doped carbon nanosheets with superior reversibility and rate capability for sodium-ion batteries, ACS Nano 11 (2017) 12658–12667.
[47] C. Liu, Q.-Q. Ren, S.-W. Zhang, B.-S. Yin, L.-F. Que, L. Zhao, X.-L. Sui, F.-D. Yu, X. Li, D.-M. Gu, Z.-B. Wang, High energy and power lithium-ion capacitors based on Mn3O4/3D-graphene as anode and activated polyaniline-derived carbon nanorods as cathode, Chem. Eng. J. 370 (2019) 1485–1492.
[48] T. Wang, Z. Kou, S. Mu, J. Liu, D. He, I.S. Amiinu, W. Meng, K. Zhou, Z. Luo, S. Chaemchuen, F. Verpoort, 2D dual-metal zeolitic-imidazolate-framework-(ZIF)-Derived bifunctional air electrodes with ultrahigh electrochemical properties for rechargeable zinc-air batteries, Adv. Funct. Mater. 28 (2018), 1705048.
[49] J. Meng, C. Niu, L. Xu, J. Li, X. Liu, X. Wang, Y. Wu, X. Xu, W. Chen, Q. Li, Z. Zhu, D. Zhao, L. Mai, General oriented formation of carbon nanotubes from metal-organic frameworks, J. Am. Chem. Soc. 139 (2017) 8212–8221.
[50] M. Kuang, Q. Wang, P. Han, G. Zheng, Cu, Co-embedded N-enriched mesoporous carbon for efficient oxygen reduction and hydrogen evolution reactions, Adv. Energy Mater. 7 (2017), 1700193.
[51] L. Zhou, C. Yang, J. Wen, P. Fu, Y. Zhang, J. Sun, H. Wang, Y. Yuan, Soft-template assisted synthesis of Fe/N-doped hollow carbon nanospheres as advanced electrocatalysts for the oxygen reduction reaction in microbial fuel cells, J. Mater. Chem. A 5 (2017) 19343–19350.
[52] Z. Hu, Z. Zhang, Z. Li, M. Dou, F. Wang, One-step conversion from core-shell metal-organic framework materials to cobalt and nitrogen codoped carbon nanopolyhedra with hierarchically porous structure for highly efficient oxygen reduction, ACS Appl. Mater. Interfaces 9 (2017) 16109–16116.

Qingyan Zhou received his B.S. degree from Harbin Institute of Technology in 2015. He is currently pursing for his Ph.D. degree in School of Chemistry and Chemical Engineering under the supervision of Prof. Zhen-Bo Wang at Harbin Institute of Technology. His research is focused the on the synthesis and characterization of carbon-based materials as highly efficiently catalysts for ORR and OER in Zn-air batteries.

Zhen Zhang received his Bachelor's degree from China University of Petroleum (East China) in 2015. He is currently pursuing his Ph.D. degree in Chemical Engineering under the supervision of Prof. Zhongwei Chen at University of Waterloo. His research is focused on the development of carbon-based porous materials towards energy storage and conversion systems, including metal-air batteries, lithium-sulfur batteries, CO_2 capture and conversion, and capacitive deionization.

Jiajun Cai received her Bachelor's degree from College of Chemistry, Jilin University in 2016. Currently, she is carrying out her Ph.D. research in School of Chemistry and Chemical Engineering at Harbin Institute of Technology under the supervision of Prof. Zhen-Bo Wang. She works on the synthesis and characterization of highly efficient catalysts for metal-air batteries.

Bing Liu received her B.S. degree from Harbin Normal University in 2017. Now she is pursing her Master's degree in Harbin Institute of Technology. Her current research focuses on the catalyst materials for Zinc-air batteries.

Yunlong Zhang received his B.S. degree in Chemical Engineering and Technology from Harbin Engineering University in 2017. He is carrying out his Ph.D. research in Harbin Institute of Technology under the supervision of Prof. Zhen-Bo Wang. Currently, he works on the synthesis and characterization of Metal Organic Frame material as high-efficiency electrocatalysts for Zinc-air battery.

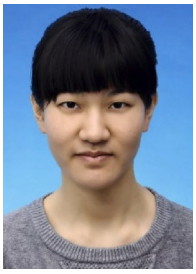

Xiaofei Gong received her B.S. degree in Chemical Engineering and Technology from Harbin Institute of Technology (Weihai) in 2015. She is carrying out her Ph.D research in Harbin Institute of Technology under the supervision of Prof. Zhen-Bo Wang. Her current researches focus on carbon-based non-noble metal catalysts for oxygen reduction reaction in fuel cells.

Dr. Xulei Sui currently is a lecturer at School of Chemistry and Chemical Engineering in Harbin Institute of Technology (HIT), China. He received his Ph.D. degree from HIT in 2015. Now he is also a postdoctoral fellow assisting Prof. Xue-Liang (Andy) Sun at University of Western Ontario, Canada and Prof. Zhen-Bo Wang at HIT. His current research interests are focused on the design and synthesis of advanced nano-materials for electrocatalysis in fuel cells.

Dr. Aiping Yu is Professor at University of Waterloo. Her research interests focus on development, processing and functionalization of nanostructured carbon materials, along with their application as electrode materials in high performance supercapacitors. She has published over 140 refereed journal papers, 3 book chapters and one book. These publications have received over 12000 citations. She holds 7 patents and provisional patents for nanomaterials or device development, and 2 of these have been licensed to industry.

Dr. Lei Zhao is currently working as a lecturer at Harbin Institute of Technology (HIT), China, meanwhile is a visiting scholar under the supervision of Prof. Zhongwei Chen at University of Waterloo. He received his B. E., M. E. and Ph.D. degree under the supervision of Prof. Zhenbo Wang at HIT in 2012, 2014 and 2017, respectively. His research interests focus on electrocatalysis, fuel cells and metal-air batteries.

Dr. Zhenbo Wang, is currently a professor of Harbin Institute of Technology. He is a distinguished professor of National 'Ten Thousand Talents' Plan Science & Technology Innovation Leader (4th batch), Ministry of Science & Technology Young Scientific & Technological Innovator and a consecutively selected for 5 years as Elsevier's "Most cited Chinese scientists". He obtained PhD degrees from HIT in 2006, and completed a post-doctoral stint at the University of Puerto Rico from 2006 to 2007. He has published more than 200 papers in peer-reviewed journals with over 5000 citations (H-index = 42). His interests lie in chemical power sources and nanoelectrode materials.

Dr. Zhongwei Chen is Canada Research Chair Professor in Advanced Materials for Clean Energy at University of Waterloo, fellow of the Royal Society of Canada and fellow of the Canadian Academy of Engineering. His research interests are in the development of advanced energy materials for metal-air batteries, lithium ion batteries and fuel cells. He has published 1 book, 7 book chapters and more than 300 peer reviewed journal articles with over 28,000 citations with H-index 81 (Google Scholar). He is also listed as inventor on 15 US/international patents, with several licensed to companies in USA and Canada. He was recipient of the 2016 E. W. R Steacie Memorial Fellowship, which followed shortly upon several other prestigious honors, including the Ontario Early Researcher Award, an NSERC Discovery Supplement Award, the Distinguished Performance and the Research Excellence Awards from the University of Waterloo.